Microchimica Acta (2019) 186: 210
https://doi.org/10.1007/s00604-019-3316-x

ORIGINAL PAPER

A hollow urchin-like α-MnO_2 as an electrochemical sensor for hydrogen peroxide and dopamine with high selectivity and sensitivity

Haiyan Song[1,2] · Hui Zhao[1] · Xianfa Zhang[1] · Yingming Xu[1] · Xiaoli Cheng[1] · Shan Gao[1] · Lihua Huo[1]

Received: 26 January 2019 / Accepted: 11 February 2019 / Published online: 2 March 2019

Abstract

A hollow urchin-like α-MnO_2 material has been synthesized by a hydrothermal method starting from $MnSO_4 \cdot H_2O$ and $(NH_4)_2S_2O_8$, and by using silver(I) as the catalyst. It has a hollow morphology with diameters of 5–6 μm and consists of densely aligned nanowires, with a 30–40 nm width and a 1.5 μm length. The diameter of the cavities and the thickness of the shell are about 1.2 μm and 300 nm, respectively. The material was placed on a glassy carbon electrode (GCE), and electrochemical experiments showed the respective sensor to possess good stability and reproducibility. The modified GCE displays response to both hydrogen peroxide (H_2O_2) and dopamine (DA) at working potentials of −0.40 V and +0.4 V, respectively (both versus SCE). H_2O_2 can be detected with an 80 nM detection limit, and DA with a 12 nM detection limit (at $S/N = 3$).

Keywords 3D hollow structure · Urchin-like α-MnO_2 · Hydrothermal synthesis · Electrocatalysis · H_2O_2 · Catalytic mechanism

Introduction

Hydrogen peroxide (H_2O_2) plays an important role in biology [1]. Dopamine (DA) is a hormone and neurotransmitter. It plays an important role in central nervous system, hormonal system and several physiological functions [2, 3]. The abnormal levels of the two components may result in disorders of neurology including schizophrenia and Parkinson's disease [4–8]. Therefore, the accurate detection of H_2O_2 and DA are extremely important. With respect of all the reported detection techniques, electrochemistry method has received great attention due to its superior selectivity, ideal sensitivity and low expensive. However, conventionally used sensors focused on biomacromolecule including enzymes and proteins present series of shortcomings such as complex construction procedures, weak stability and shorter lifetime. Thus, the non-enzyme electrochemical sensors, based on transition metal oxides nanomaterials, come into being [9].

Manganese dioxide (MnO_2), a typical transition metal oxide, has become an interesting and well-studied material in many fields because of the novel chemical and physical properties as a result of its excellent structural flexibility [10]. Based on various linkage means of basic [MnO_6] octahedral units, MnO_2 possess different types of polymorphs, such as α, β, γ and δ. Among them, α-MnO_2 shows ideal catalytic activities, due to the occurrence of edge-sharing MnO_6 octahedral, which lead to the formation of 1D (2 × 2) and (1 × 1) tunnels extended in a direction parallel to the c-axis of the tetragonal unit cell via linking at corners [11]. Until now, various morphologies of MnO_2 like zero-dimensional (0D) nanoparticles [12], one-dimensional (1D) nanotubes [13], nanorods [14], nanowires [15], and two-dimensional (2D) nanosheets [16] have been successfully synthesized and

Electronic supplementary material The online version of this article (https://doi.org/10.1007/s00604-019-3316-x) contains supplementary material, which is available to authorized users.

✉ Yingming Xu
xuyingming@hlju.edu.cn

✉ Lihua Huo
huolihua@hlju.edu.cn

[1] Key Laboratory of Functional Inorganic Material Chemistry, Ministry of Education, School of Chemistry and Materials Science, Heilongjiang University, Harbin 150080, China

[2] Laboratory of Test Center, Jilin Agricultural Science and Technology College, Jilin 132101, China

characterized. For better performance, much attention has been paid to the incorporation of all the above structures as blocks into 3D complex structures such as nanoflowers [17], microspheres [18] and dandelion- and urchin-like [10]. At present, the application of MnO_2 in electrocatalysis is mainly focused on nanosheets, in which the lowest detection limit of H_2O_2 is mostly 10^{-7} mol·L^{-1} [19], and dopamine is 10^{-8} mol·L^{-1} [20]. There is still possibility to improve the catalytic performance of α-MnO_2 to H_2O_2 and dopamine, compared with other metal oxides sensors. In general, larger specific surface areas as well as more active sites are important to further improvement of the catalytic performance. In view of the outstanding performance of hollow structural materials in the field of batteries and supercapacitors [21, 22], it is hoped that electrocatalysis, which also belongs to the field of electrohemistry, should have similar characteristics and properties. However, MnO_2 with the hollow structure were rarely reported [10, 18, 23], mainly used in gas sensor [23], oxygen reduction reaction and oxygen evolution reaction [10]. It might be restricted by the synthesis conditions, the poor monodispersion of these hollow MnO_2 (dandelion- and urchin-like). In addition, a few literatures on the detailed catalytic mechanism of MnO_2 for H_2O_2 and DA can be found till today, except for some rough descriptions in papers [4, 9, 24, 25]. Based on these considerations, we intend to synthesize a kind of MnO_2 with uniform and well-dispersed hollow 3D structure and apply them in electrocatalysis of small molecules, such as H_2O_2, DA and others. Furthermore, the catalytic mechanism of MnO_2 for small molecules will be also investigated.

Herein, we describe a more attractive hollow urchin-like α-MnO_2 which was successfully synthesized via hydrothermal method. This unique hollow structure has a high specific surface area which is helpful for increasing active sites. Taking the above advantage into consideration, the hollow urchin-like α-MnO_2 was chosen to construct a electrochemical sensor for detecting H_2O_2 and DA in phosphate buffer (pH = 7.4) without interference of some coexistence components such as Biogenic Amines, ascorbic acid (AA) and uric acid (UA). This is the first report that the hollow urchin-like α-MnO_2 sensor was fully applied to the determination of H_2O_2 and DA through electrocatalysis, with rapidity (short response time), high sensitivity and selectivity. Beyond that, both the catalytic mechanism of MnO_2 for H_2O_2 and DA was investigated respectively.

Experimental

Reagents

Dopamine (DA), ascorbic acid (AA), and uric acid (UA) were purchased from Sigma Aldrich Co., USA (https://www.sigmaaldrich.com/china-mainland.html). Adrenaline, Histamine, Epnephrine, Serotonin, Tyramine and Phenethylamine were purchased from Shanghai Titan Scientific Co., Shanghai, China (http://www.titansci.com/index.action). $MnSO_4·H_2O$, $AgNO_3$, chitosan (cs), and $(NH_4)_2S_2O_8$ were all analytical grade reagents and bought from Beijing Chemical Reagent Co., Beijing, China (http://www.crc-bj.com/); H_2O_2, KH_2PO_4 and K_2HPO_4 were purchased from Tianjin Tianli Chemical Reagent Co., Tijian, China (http://9211251.582582.com/). H_2O_2 aqueous was freshly prepared before use. Phosphate buffer (0.05 mol·L^{-1}, pH 7.4) composed of KH_2PO_4 and K_2HPO_4 was the supporting electrolyte.

Instrumentation

X-ray diffraction meter was employed to investigate the urchin-like α-MnO_2 nanospheres with Cu *Kα* radiation (λ = 1.5406); Bragg angle range from −10 to 80 deg. (XRD; D/MAX-III-B-40KV, Japan).

The structure of the samples was characterized by transmission electron microscope under 200 kV acceleration voltage (TEM; JEOL-2100, JEOL Co., Japan).

Microstructure of urchin-like α-MnO_2 was investigated with scanning electron microscope, under the operational power of 15.0 kV (SEM; Hitachi S-4800, Hitachi, Japan).

All the electrochemical tests were conducted on a electrochemical workstation equipped with standard three-electrode system (CHI-760E, Shanghai Chenhua Apparatus Co., Shanghai, China, http://chi.instrument.com.cn), in which the diameter of modified glassy carbon electrode (GCE; the working electrode) was 5 mm; the auxiliary electrode and reference electrode were platinum wire and saturated calomel electrode (SCE), respectively. Electrochemical impedance spectroscopy (EIS) and Cyclic Voltammograms (CV) were investigated in 5 mmol·L^{-1} $[Fe(CN)_6]^{-3/-4}$ (1:1) containing 0.1 mol·L^{-1} KCl; Chronocoulometry used for determining the apparent electrode areas with different modification was conducted in 1 mmol·L^{-1} $K_3Fe(CN)_6$ with 2 mol·L^{-1} KCl. Chronoamperometry was applied to the catalytic response, interference measurement and analysis of the biological samples in Phosphate buffer (0.05 mol·L^{-1}, pH 7.4).

Synthesis of hollow urchin-like α-MnO_2

The hollow urchin-like α-MnO_2 was synthesized as reported in literature with some modifications [18]. In brief, $MnSO_4·H_2O$ (0.270 g), $(NH_4)_2S_2O_8$ (0.365 g) and 1.6 mL of con.H_2SO_4 were added to deionized water of 40 mL at 25 °C. Then, 0.8 mL of $AgNO_3$ (5.9 mol·L^{-1}) solution was put into the above solutions. When the stirring was lasted for 30 min, the resulting mixture was put into Teflon-lined stainless steel autoclave with a volume of 50 mL. After sealed tightly, the steel autoclave was heated for 6 h under the temperature of 120 °C. When the reaction was finished, the

resulting black precipitate sample was collected by centrifugation, then washed using deionized water and ethanol, and dried for 12 h at the temperature of 80 °C in an oven.

Preparation of different modified glassy carbon electrodes (GCEs)

GCE (d = 5 mm) was polished via using different size of alumina slurry (0.3, 0.1 and 0.05 μm) consecutively, it was then treated by ultrasound wave in 50% nitric acid aqueous, absolute ethanol and deionized water, successively. Thereafter, the electrode was activated in 0.25 mol·L^{-1} H_2SO_4 by the cycled (20 cycles) potential ranged from −1.0 to - 1.0 V. Then, 10 μL of urchin-like α-MnO_2 dispersion with the concentration of 5 mg·mL^{-1} was slowly dropped onto the surface of GCE. Subsequently, 5 μL of 2% (wt.) chitosan solution was added onto the electrode mentioned above. Each modification must be dried in air. The rest modified electrodes were all constructed by using the corresponding dispersions material.

Results and discussion

Characterization of the nanocomposites

The composition and phase purity of sample obtained at 120 °C (6 h of reaction time) was characterized by XRD. As shown in Fig. 1a, all the diffraction peaks can be clearly matched to pure phase of α-MnO_2 with tetragonal (JCPDS 44–0141). Furthermore, the peaks of 28.9°, 37.6° and 56.8° present the largest intensity, it implies the resulting MnO_2 material is abundant in (310), (211) and (600) crystalline planes. No peaks can be observed for amorphous MnO_2. This confirms the high purity and crystallinity of the material.

The direct information related to structure as well as morphology of the synthesized product mentioned above can be obtained from the SEM and TEM at various magnification. As shown in Fig. 1b, hollow urchin-like microspheres with cavities can be observed clearly. The diameter of the cavities and the thickness of the shell are about 1.2 μm and 300 nm respectively. The magnified image shows that the urchin-like microspheres is assembled by much densely packed and spherically aligned smooth nanowires with the length and diameter of approximately 1.5 μm and 30–40 nm, respectively (Fig. 1c). By observing TEM images, further verifying the hollow morphology of the urchin-like microspheres with diameter of 5–6 μm (Fig. 1d), in accordance with the SEM observation from Fig. 1c . HRTEM image is shown in Fig. 1e, from which the lattice spacing is calculated to be 0.233 nm, in agreement with the (211) planes of the MnO_2. This result is corresponding to that of XRD technique.

To further know the porous structure and specific surface area of urchin-like α-MnO_2, N_2 adsorption and desorption measurements were conducted (Fig. 1f). According to the IUPAC classification, the α-MnO_2 exhibits a type IV isotherm with H3 type hysteresis loop. The distribution curve of α-

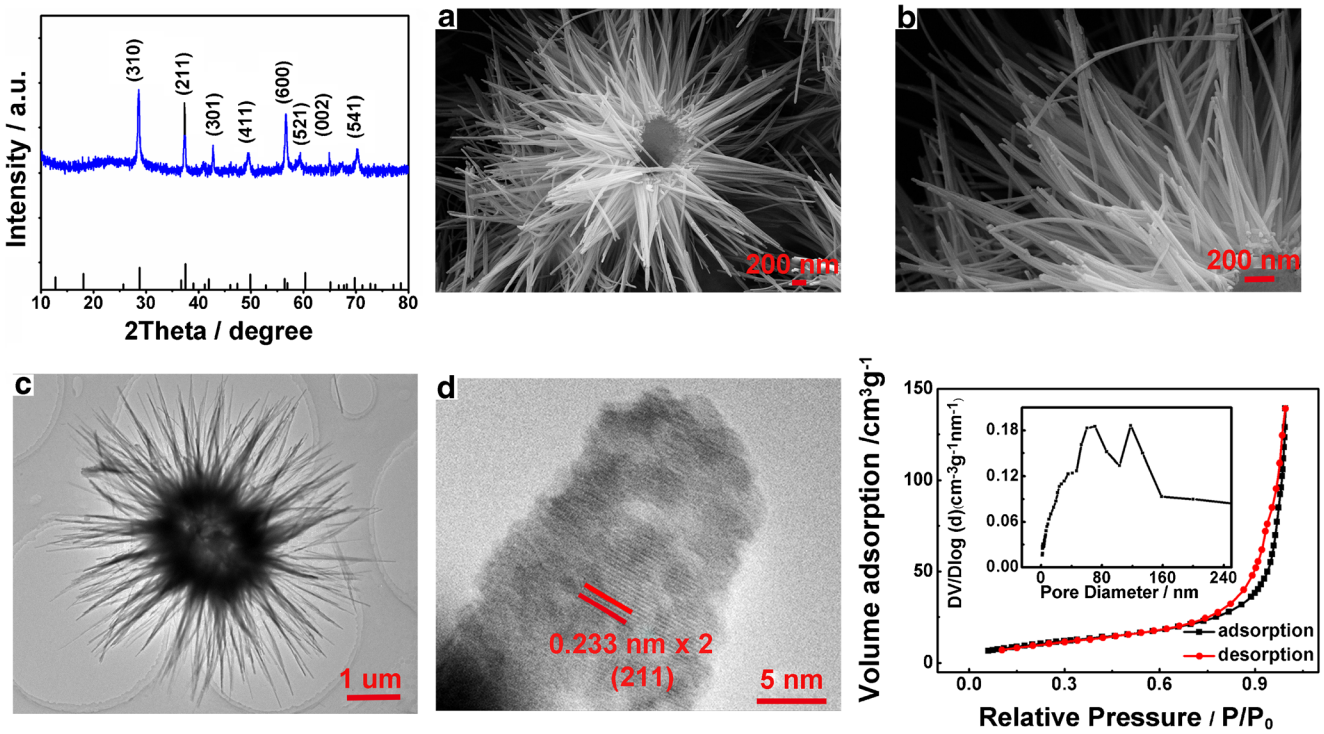

Fig. 1 XRD patterns (**a**), SEM (**b**, **c**), TEM (**d**), HRTEM (**e**) images, N_2 adsorption-desorption isotherms (**f**) and pore size distribution plot (inset of f) of urchin-like α-MnO_2 synthesized at 120 °C for 6 h

MnO_2 pore size shows that the main pore sizes are 70 nm and 120 nm which come from the cross stacking of the nanowires on urchin-like microsphere. The specific surface area is 47.23 m^2 g^{-1}, which provided a potential for excellent electrochemical properties.

Growth mechanism of hollow urchin-like α-MnO_2

The influence of the reaction temperature (60, 90, 120,150 and 180 °C) on the microstructure of the products has also been investigated. As shown in Fig. S1 (Supplementary material), the planes and crystallinity of the synthesized particles vary following with the change of reaction temperature, and ideal uniform hollow urchin-like microspheres of α-MnO_2 with more planes and better crystallinity can be found when the temperature reaches to 120 °C under the reaction time of 6 h. Hence, the optimal reaction temperature for synthesizing hollow urchin-like α-MnO_2 should be fixed at 120 °C.

To investigate the growing process of urchin-like α-MnO_2, time-dependent experiments were carried out at 120 °C and monitored by SEM, and the result is displayed in Fig. 2. It shows that there are a large amount of inhomogeneous microspheres with rough surface at 2 h of reaction time (Fig. 2a). With the reaction time increases to 4 h, the glitch of the particle surface becomes longer compared with that of obtained from the time of 2 h (Fig. 2b). The prototype of urchins can be observed from most of particles. When reaction time is continuously increased to 6 h, the interesting uniform hollow urchin-like microspheres form completely (Fig. 2c). In view of experimental results mentioned above, the reaction time is further lengthened to 8 h, excessive nanowires can be found clearly on the tip of nanowires of urchins, like a network covering the urchin and interwoven (Fig. S2, Supplementary material). This is very similar to the formation process of α-MnO_2 products with the increase of the temperature. XRD patterns of α-MnO_2 were also investigated within various reaction times. As shown in Fig. S3 (Supplementary material), the α-MnO_2 synthesized around 6 h exhibits more planes and better crystallinity compared with the samples obtained at other reaction times. The trend of the intensity of diffraction peaks and the crystallinity are also similar to that of samples obtained at increasing temperatures. It indicates that the crystallinity of the materials is closely concerned to the microstructure of materials. Finally, optimal reaction time and temperature for synthesizing hollow urchin-like α-MnO_2 should be around 6 h at 120 °C.

Based on time-dependent stuctures and morphologies of nanostructured α-MnO_2 mentioned above, an "Ostwald ripening process" can be introduced to give a reasonable explanation on the phenomena. At the beginning, lots of nuclei arise within a short time with the aid of the reaction between $MnSO_4 \cdot H_2O$and $(NH_4)_2S_2O_8$. Subsequently, the nuclei gradually aggregate to form the microspheres, belongs to a solid cores. Then, MnO_2 nanowires would gradually evolve from the above spherical aggregates owing to the one-dimension growth habit. Finally, an interior cavity formed by means of a core evacuation procedures following with the continuous increase of reaction time, which may be the result of higher surface energies [23].

Selection of the experiment conditions

The optimal applied potential used in this work is chosen according to comparision of amperometric response to equal amount of H_2O_2 and DA (Fig. S4, Supplementary material). The applied potentials of −0.2 V, −0.3 V, −0.4 V and − 0.5 V were investigated in the study of H_2O_2, and the tested potential for DA was 0.2 V, 0.3 V, 0.4 V and 0.5 V, respectively. Based on the consideration of the increases of catalytic current

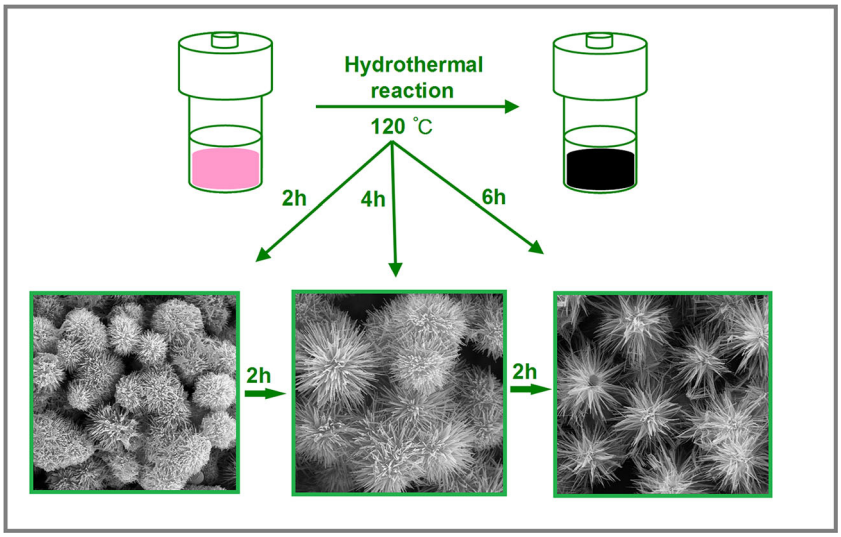

Fig. 2 Diagram of the formation for urchin-like α-MnO_2 and corresponding morphology: (**a**) 2 h; (**b**) 4 h; (**c**) 6 h

and noise current, the optimal applied potential of H_2O_2 and DA are determined to be −0.4 V and 0.4 V, respectively.

The effect of different pH (5.6, 6.2, 6.8, 7.4, 8.0 and 8.6) of phosphate buffer on catalytic response for equal H_2O_2 and DA were also investigated. As shown in Fig. S5 and Fig. S6 (Supplementary material), the catalytic current of H_2O_2 and DA in the system (pH = 7.4) is larger than those of other five pH, thus, 7.4 is chosen as the optimal pH in the larter experiments.

The modifier content of α-MnO_2 (5, 10, 15, and 20 μL) on the GCE was also investigated. As shown in Fig. S7 (Supplementary material), the catalytic currents of 10 μL are the largest for equal amount of H_2O_2 and DA among the four modifier content. Therefore, 10 μL is chosen as the optimal modifier content.

Electrochemical properties of the constructed electrodes

In order to study the relationship between microstructure of sensing materials and catalyzation, five sensors were fabricated based on different MnO_2 synthesized at different temperatures (60, 90, 120, 150 and 180 °C). Responses of the five sensors to 0.4 mmol·L^{-1} H_2O_2 were measured in 0.05 mol·L^{-1} phosphate buffer (pH 7.4). As shown in Fig. S8 (Supplementary material), the structure of hollow urchin-like MnO_2 synthesized at 120 °C possesses the highest catalytic current compared with those of other four sensors. Similar experiments were also carried out, in which the responses to DA are consistent with the results to H_2O_2. It suggests that the uniform and hollow urchin-like structures possess larger specific surface as well as more active sites. Hence, the MnO_2 synthesized at 120 °C is selected to construct sensor in this work.

EIS and CV methods were applied to investigate the electrochemical characterization of three kinds of electrodes including GCE (a), cs/α-MnO_2/GCE (b) and α-MnO_2/GCE (c) (Fig. 3a and b). Interface properties of the different electrodes can be gained from EIS. The semicircle diameter appeared at higher frequencies relates to procedures concerning to electron transfer-limited, in which the diameter of the semicircular plot is dependent on electron-transfer resistance [1]. As can be seen from Fig. 3a, after the electrode was modified, the electron transfer resistance varies accordingly. A plot with effectively linear can be clearly found using GCE (curve (a)). When GCE is covered by α-MnO_2, the corresponding semicircle of the plot increases significantly as expected (curve (c)). The reason may be the negative charge of α-MnO_2 surface has repulsive effect on that of $[Fe(CN)_6]^{3-}$ probe molecules to some extent. When cs is introduced, the semicircle of the plot is reduced in comparison to that of α-MnO_2 modified electrode (curve (b)). This presumably because negatively charged probe molecules was adsorbed and accumulated to the cs film with positive charge [1]. The corresponding electron-transfer resistance of different electrodes increases following the order of GCE(84.7 Ω) < cs/α-MnO_2/GCE (324.7 Ω) < α-MnO_2/GCE(509.5 Ω). The capacitance of different modified electrodes can be calculated using the Eq. 1 [26]:

$$C_i = \frac{(R_i Q_i)^{\frac{1}{n_i}}}{R_i} \quad (1)$$

where C_i is the capacitance; R_i is the electron-transfer resistance of the modified electrode; Q_i and n_i are the parameters of a constant phase element. The C_i value of cs/α-MnO_2/GCE is 2.05×10^{-6}. The relevant parameters of GCE and α-MnO_2/GCE have been listed in Table S1.

To confirm whether there are some changes of electrode behavior among different electrodes, CV experiments were also carried out. As shown in Fig. 3b, the peak current of CV decreases following the order of GCE > cs/α-MnO_2/GCE > α-MnO_2/GCE, which is justly opposite to that of electron-transfer resistance, indicating that there is the change of electrode behavior among different electrodes. For drawing a same conclusion on the change of electrode behavior among different electrodes, there must be an opposite tendency with regard to electron-transfer resistance and CV peak current.

In order to prove the effect of different electrodes on apparent electrode areas, chronocoulometric plots that collected from the reduction of $K_3Fe(CN)_6$ (1.0 mmol·L^{-1}) in KCl (2.0 mol·L^{-1}) were plotted using three kinds of electrodes studied in this work. The corresponding equation is (Eq. 2) [27]:

$$Q = \frac{2nFAcD^{1/2}t^{1/2}}{\pi^{1/2}} + Q_{dl} + Q_{ads} \quad (2)$$

where Q represents the absolute value of reduction charge, n presents electrons transferred number, F is the Faraday constant, A is apparent electrode area and t is time; c is the bulk concentration of oxidized form of the hexacyanoferrate (III) complex, while D is the corresponding diffusion coefficient in comparison to C (7.6×10^{-6} $cm^2 \cdot s^{-1}$); Q_{dl} is double-layer charge and Q_{ads} is Faradic charge. The apparent electrode area (A) can be calculated via the slope of Q versus $t_{1/2}$ plot. As shown in Fig. 3c, the slope values increase following with the order of GCE < α-MnO_2/GCE < cs/α-MnO_2/GCE and the corresponding apparent electrode areas are 0.14, 0.24 and 0.26 cm^2, respectively. The effective surface area of cs/α-MnO_2/GCE is approximately 1.86 times larger than that of GCE, indicating that urchin-like α-MnO_2 composites possess a promising electrochemical performance due to the lager value of A.

CV curves of the constructed cs/α-MnO_2/GCE electrode in H_2O_2 aqueous (0.1 mmol·L^{-1}) were also tested at a designed scan rates (Fig. 3d). The oxidation peak current gradually increases with the increasing of scan rate within 50–500 mV·s^{-1} (inset of Fig. 3d); the associated current-scan rate relationship is: $I = 0.011\ v - 0.71$ ($R^2 = 0.99$). Based on the Semerano criterion, it can be known that electro-reduction of

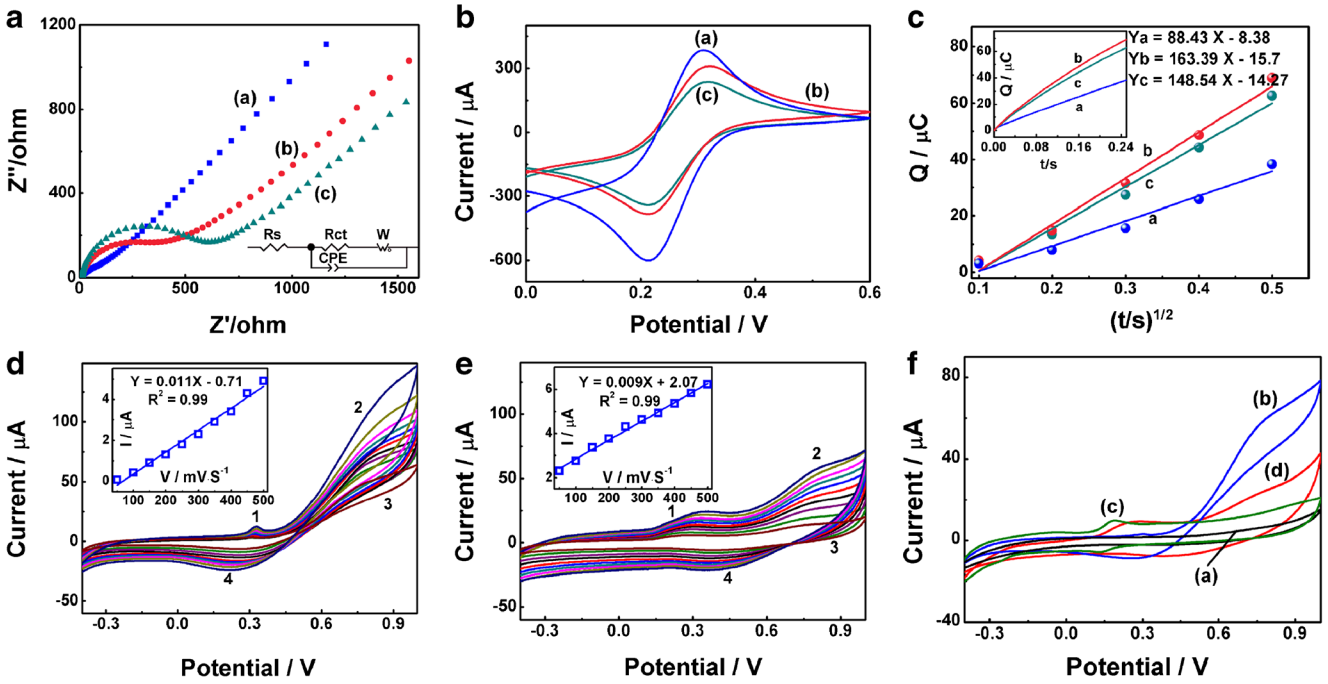

Fig. 3 Electrochemical properties exhibited by modified electrodes: (**a**) - EIS (Randles equivalent circuit for EIS, inset) and (**b**) - CV in 5 mmol·L^{-1} $[Fe(CN)_6]^{-3/-4}$ (1:1) + 0.1 mol·L^{-1} KCl; (**c**) - the curves of Q-t$^{1/2}$ and Q-t (inset) for reduction of 1 mmol·L^{-1} $K_3Fe(CN)_6$ in 2 mol·L^{-1} KCl; CVs of the cs/α-MnO_2/GCE in phosphate buffer (pH 7.4) at various scan rates (50–500 mV·S^{-1}, inside and out) under addition of (**d**) H_2O_2 (0.1 mmol·L^{-1}) and (**e**) DA (0.01 mmol·L^{-1}). Inset: oxidation peak currents vs. the scan rates; (**f**) - CV responses of different modified electrodes to H_2O_2 and DA (a - cs/α-MnO_2/GCE in phosphate buffer (pH 7.4); b - cs/α-MnO_2/GCE to 0.1 mmol·L^{-1} H_2O_2; c - GCE to 0.01 mmol·L^{-1} DA and d - cs/α-MnO_2/GCE to 0.01 mmol·L^{-1} DA)

H_2O_2 is mainly a surface-confined process. The number of electron transferred in the reaction can be calculated by the Laviron's equations (Eq. 3):

$$I_p = \frac{n^2F^2\upsilon A\Gamma_T}{4RT} = \frac{nFQ\upsilon}{4RT} \quad Q = nFA\Gamma_T \tag{3}$$

where n presents electrons transfer number, Q is the peak area and v is the corresponding scan rate. Based on the relationships of I_p versus v, the values of n are in the range of 1.67–1.82, therefore, the values of n are approximately 2.

As shown in Fig. S5a (Supplementary material), the anodic peak potential of H_2O_2 is linearly proportional to the pH value (from 5.6 to 8.6) with the equation of $E_p = -0.057$ pH + 0.73 ($R^2 = 0.98$). The slope is 0.057, which is close to 0.059 V/pH, indicating that the number of electron-transfer and protons taking part in the reaction are equal. Beyond that, the charge-transfer coefficient was also calculated. The corresponding equation (Eq. 4) was listed as follows.

$$E_p = E_0 + \frac{RT}{(1-\alpha)nF}\ln\upsilon \tag{4}$$

where α is the charge-transfer coefficient and others have same meanings as mentioned above. It can be seen that the E_p - ln$V$ for H_2O_2 is $E_p = 0.013$ ln$V$ + 0.33 ($R^2 = 0.98$) (Fig. S5b, Supplementary material). The value of α is calculated to be 0.05. The standard heterogeneous transfer (k_s) of H_2O_2 on cs/α-MnO_2/GCE is 2.36 s^{-1}, which is calculated according to Eq. 5 [27]:

$$\ln k_s = \alpha\ln(1-\alpha) + (1-\alpha)\ln\alpha - \ln\frac{RT}{nF\upsilon} - \frac{(1-\alpha)\alpha F\Delta E_p}{RT} \tag{5}$$

The above experiment was also conducted in 0.01 mmol·L^{-1} DA (Fig. 3e). The corresponding current-scan rate relationship is: $I = 0.009\ v + 2.07$ ($R^2 = 0.99$), demonstrating that the oxidation of DA is also a surface-confined process. The relation of E_p-pH is $E_p = -0.053$ pH +0.66 ($R^2 = 0.98$), indicating that the number of electron-transfer and protons taking part in the reaction of DA are equal (Fig. S6a, Supplementary material). According to Eq. 3, the values of electron-transfer number of DA on the cs/α-MnO_2/GCE are in the range of 1.72–1.94, it is also approximately 2. According to the calibration of $E_p = 0.034$lnV + 0.33 ($R^2 = 0.98$) (Fig. S6b, Supplementary material) and Eq. 4, the charge-transfer coefficient α is 0.62. The standard heterogeneous transfer (k_s) of DA on cs/α-MnO_2/GCE is 2.68 s^{-1}.

Catalytic mechanism of the modified electrode

The mechanism for reduction of H_2O_2 on modified electrode was investigated. As shown in Fig. 3f, no peak can be observed on cs/α-MnO_2/GCE in phosphate buffer (curve a), however, four peaks can be obviously found after addition

of H_2O_2 (curve b). The reason may be resulted from the reaction of H_2O_2 and α-MnO_2 modified on the GCE. According to the published work [24], the procedure is that H_2O_2 is firstly adsorbed onto the surface of α-MnO_2 which is then reduced to low valence states. Subsequently, Mn of low states mentioned above are oxidized back to MnO_2 at the surface of electrode. With the addition of H_2O_2, Mn species in the form of trivalent and bivalent including $Mn(OH)_2$ and Mn_2O_3 arise. (Eqs. 6 and 7). After the electrooxidation process, the Mn of low states formed above are changed into MnO_2 again (Eqs. 8 and 9). According to the potential diagram exhibited by Mn, the redox couple of Mn(III)-Mn(IV) should correspond to Peak 1 (Eq. 7), and that of Mn(II)-Mn(IV) should match to peak 2 (Eq. 6). According to the numbers of transferred electrons and protons, the reaction mechanism of H_2O_2 on the cs/α-MnO_2/GCE can be speculated as follows:

$$MnO_2 + H_2O_2 \rightarrow Mn(OH)_2 + O_2 \quad (6)$$

$$2MnO_2 + H_2O_2 \rightarrow Mn_2O_3 + O_2 + H_2O \quad (7)$$

$$Mn(OH)_2 \rightarrow MnO_2 + 2H^+ + 2e^- \quad (8)$$

$$H_2O + Mn_2O_3 \rightarrow 2MnO_2 + 2H^+ + 2e^- \quad (9)$$

To explore the catalytic mechanism of the DA on the cs/α-MnO_2/GCE, CV experiments were also done. As revealed in Fig. 3f, a 0.187 V (curve (c)) of oxidation peak potential of DA on GCE can be clearly found. The CV was further conducted in phosphate buffer containing DA using cs/α-MnO_2/GCE, the oxidation peak potential is 0.273 V (curve (d)). Based on the experimental results in H_2O_2 aqueous, peak potential of Mn(III)-Mn(IV) appears at 0.301 V (curve (b)). The oxidation peak potential (0.273 V) of cs/α-MnO_2/GCE for DA is between the two potentials mentioned above, which may be caused by superposition of the two peaks. Moreover, the peak potential of 0.766 V is just corresponding to Mn(II)-Mn(IV). In combination with existing report [27] and the numbers of transferred electrons and protons, the possible reactions of DA on the cs/α-MnO_2/GCE can be described as follows:

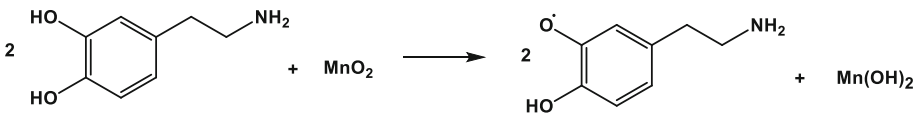

(10)

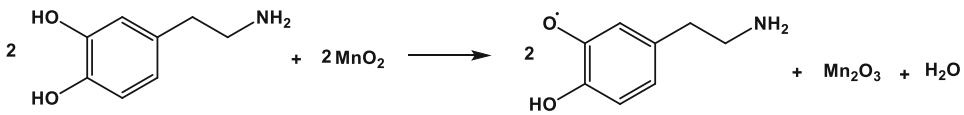

(11)

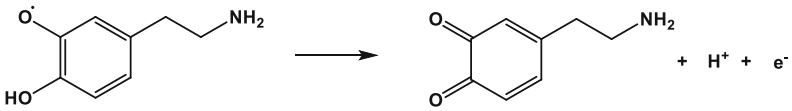

(12)

$$Mn(OH)_2 \rightarrow MnO_2 + 2H^+ + 2e^- \quad (13)$$

$$Mn_2O_3 + H_2O \rightarrow 2MnO_2 + 2H^+ + 2e^- \quad (14)$$

Electrocatalysis of H_2O_2 and DA at the cs/α-MnO_2/GCE

To investigate the catalytic performance of cs/α-MnO_2/GCE, amperometric experimenst to different aliquots of H_2O_2 was operated using phosphate buffer (pH 7.4) as the buffer system at −0.4 V (Fig. 4a). When H_2O_2 was brought to the electrochemical cell, it can be clearly seen that the reduction current increase rapidly. Only within 5 s, the steady-state current (approximately 95% levels) almost achieved. This nonenzymatic H_2O_2 sensor shows two linear ranges; one within 0.24 μmol·L^{-1}- 0.10 mmol·L^{-1} exhibits a high sensitivity and desirable correlation coefficient (R^2) of 0.55 μA (μmol·L^{-1})$^{-1}$ cm $^{-2}$ and 0.99, and the other one ranged from 0.10 to 6.67 mmol·L^{-1} also possesses an excellent R^2 (0.99). The detection limit is 80 nmol·L^{-1} at the signal-to-noise ratio of 3.

Instead of H_2O_2, DA was also conducted at the cs/α-MnO_2/GCE in the stirred electrolyte solution at 0.4 V (Fig. 4c). This DA sensor shows an excellent linear relationship in the range of 0.05 μmol·L^{-1} to 88.8 μmol·L^{-1} with a high sensitivity and desirable correlation coefficient (R^2) of 8.35 μA (μmol·L^{-1})$^{-1}$

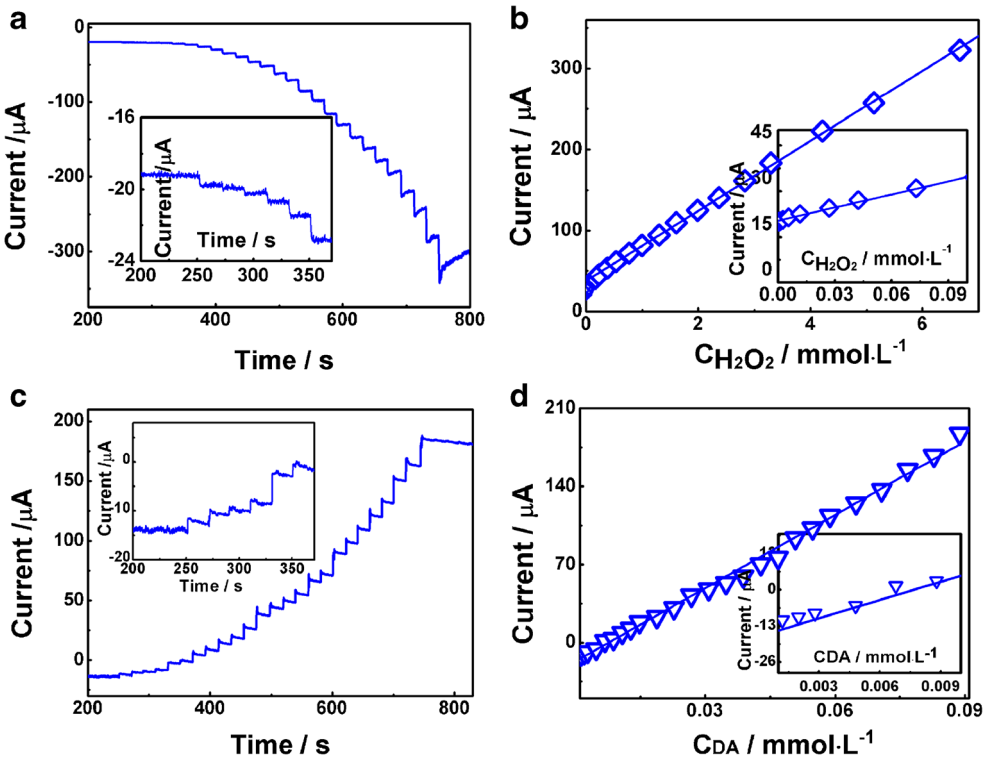

Fig. 4 Current responses obtained from cs/α-MnO_2/GCE in series of additions of (**a**) H_2O_2 and (**c**) DA dissolved in phosphate buffer (pH 7.4). Applied potential to H_2O_2 and DA are −0.4 V and 0.4 V, respectively. (vs. SCE). Inset: magnified plot of the small ladders. Calibration plot of the cs/α-MnO_2/GCE modified electrode as a function of (**b**) H_2O_2 and (**d**) DA concentration. Inset: magnified plot of low analyte concentrations

Table 1 Comparison of the DA and H_2O_2 determination with different modified electrodes previously reported in the literatures

Electrode	Linear range		Detection limit		Ref.
	H_2O_2 (mmol·L^{-1})	DA (μmol·L^{-1})	H_2O_2 (nmol·L^{-1})	DA (nmol·L^{-1})	
PTCA-RGO-MWCNTs-AuNPs/GCE	-*	1-100	–	70	[2]
δ-MnO_2/CNTs	0.05–22	–	1000	–	[4]
Au/pBDD	–	0.1–1000	–	60	[5]
P/CoS_2 /IL-GN/GCE	–	0.1–400	–	40	[6]
NP-PtY/GR/ GCE	–	0.9–82	–	360	[7]
OFMs/GCE	–	0.2–115	–	30	[8]
MnO_2/rGO/GCE	0.01–0.09 0.2–0.9	–	2000	–	[9]
MnO_2 NTs/RGO NCs	0.1–80	–	820	–	[13]
NGNF/MnO_2	0.1–11	–	1250	–	[14]
MnO_2/ERGO paper	0.1–45.4	–	10,000	–	[15]
MnO_2/CF	0.0025–2.055	–	120	–	[19]
MnO_2-RGO	–	0.06–1.0 1.0–80	–	1.0	[20]
MnO_2/SWCNT-Nf/GCE	0.005–3	–	520	–	[24]
MnO_2/rGONRs/GCE	0.00025–2.245	–	71	–	[28]
Ag/MnO_2/GO	0.003–7	–	700	–	[29]
MnO_2/RGO/P_{25}	0.001–4	–	300	–	[30]
MnO_2/Vertically aligned MWCNTs/Cu	0.0012–1.8	–	800	–	[31]
β-MnO_2	–	0.03–65	–	8.2	[32]
DAAO-Hb/MnO_2 NPs/PTh	–	0.04–9	–	41	[33]
3D Pt/RGO/MnO_2	–	1.5–215.56	–	100	[34]
NPG-μE	–	0.1–10	–	30	[35]
GCE/P-Arg/ErGO/AuNP	–	0.001–0.05 1.0–50	–	1	[36]
Na_4(CuTCPP)-rGO/GC	–	0.0024–3.6	–	0.8	[37]
cs/α-MnO_2 /GCE	0.00024–0.1 0.1–6.67	0.05–88.8	80	12	This work

*- represents the analyzed compound did not be detected using the modified electrode

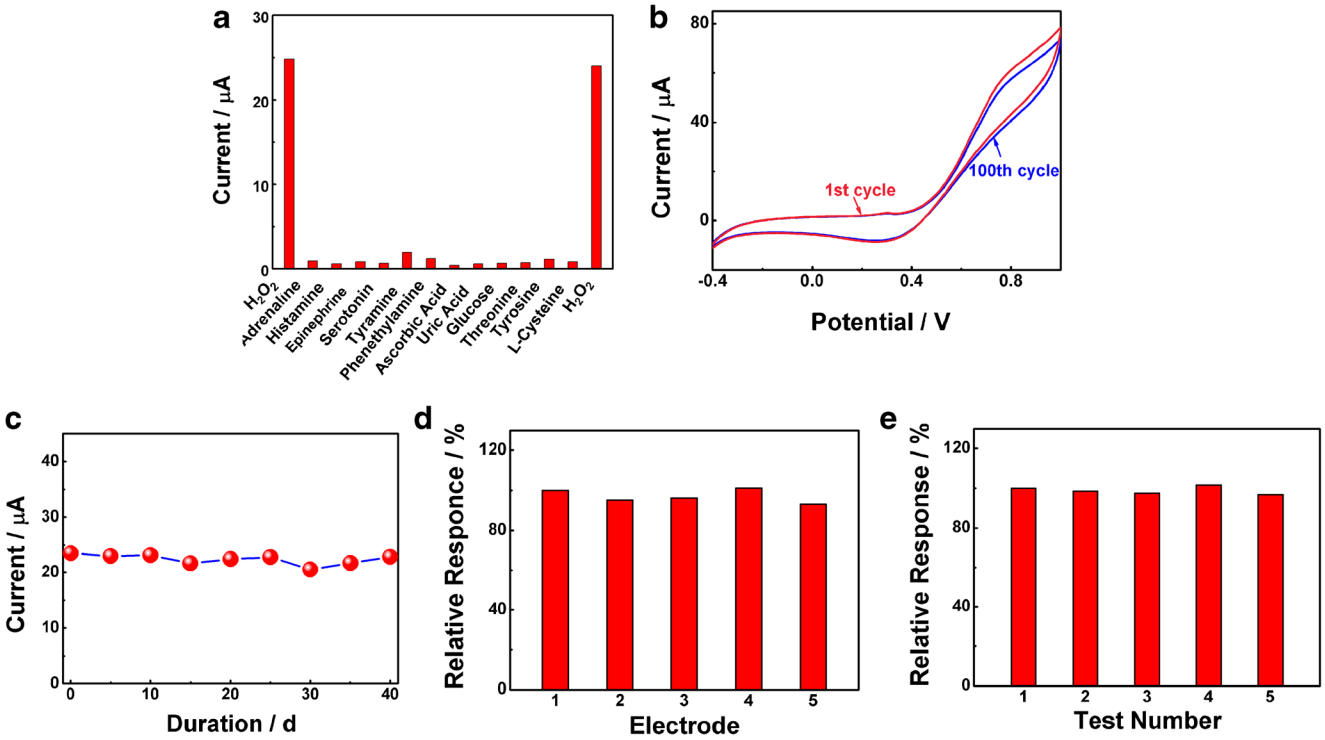

Fig. 5 **a** - Interference study in the presence of 0.04 mol·L^{-1} H_2O_2 and 0.6 mol·L^{-1} interfering chemicals; **b** - the 1st and 100th CV curves; **c** - the currents of electrode during 40 days storage; **d** - reproducibility studies with 5 electrodes and **e** - five consecutive measurements of cs/α-MnO_2/GCE towards 0.1 mol·L^{-1} H_2O_2 in phosphate buffer (pH 7.4). Applied potential: −0.4 V (vs. SCE)

cm $^{-2}$ and 0.99. The detection limit is 12 nmol·L^{-1} at S/N of 3. In order to confirm the suitability of the constructed sensor in practical industry, the comparison experiments were also conducted. The results show that the current without N_2 (curve b) reaches 97% of that in N_2 saturated system (curve a) (Fig. S10, Supplementary material), indicating that the difference caused by dissolved oxygen can be neglected in the range of the errors permitted. The property of cs/α-MnO_2/GCE to DA and H_2O_2 is compared with those of related work reported in previous literatures (Table 1). The electrode assembled in this work performs at least as well or somewhat better in comparison to some other studies. The desirable properties of cs/α-MnO_2/GCE to H_2O_2 and DA may be the result of relatively larger surface/volume ratio of urchin-like α-MnO_2 microspheres, which promotes the adsorption of H_2O_2 and DA. Furthermore, the increasing of the active sites also plays an important role.

Selectivity, stability and reproducibility of the constructed electrode

To evaluate the selectivity of the method in this study, potential interferences material, including amino acids (Threonine, Tyrosine and L-cysteine), biogenic amines (epinephrine, adrenaline, histamine, serotonin, tyramine and phenethylamine), ascorbic acid (AA), uric acid (UA) and glucose were tested. The interference experiments of H_2O_2 and DA were performed

Table 2 Determination of H_2O_2 and DA in biological samples using the α-MnO_2 modified GCE

Sample	Hydrogen peroxide (μmmol·L^{-1})			Dopamine (μmmol·L^{-1})		
	Added	Found[a]	Recovery(%)[b]	Added	Found[a]	Recovery(%)[b]
Serum	50	47.2 ± 1.2	94.7 ± 2.3	20	18.6 ± 0.7	92.7 ± 3.1
	100	97.3 ± 0.9	97.3 ± 0.9	40	38.4 ± 0.8	96.1 ± 1.9
	150	147.4 ± 0.9	98.3 ± 0.6	60	57.9 ± 0.6	96.6 ± 0.9
Urine	50	47.4 ± 0.7	94.8 ± 1.4	20	18.7 ± 0.8	93.2 ± 3.4
	100	97.1 ± 1.1	97.1 ± 1.1	40	38.2 ± 0.7	95.5 ± 1.8
	150	147.5 ± 1.4	98.4 ± 0.9	60	57.9 ± 1.2	96.5 ± 1.9

[a] Found = mean ± S.D. (n = 3) and RSD were all lower than 3.5%

[b] Recovery = mean ± S.D. (n = 3) and RSD were all lower than 4.0%

separately due to different applied potentials (Fig. 5a and Fig. S9a, Supplementary material). The results reveal that the competitors have no influence on the excellent selectivity of the modified electrode assembled in this work even if they were presented in 15-fold concentrations. All these prove that the fabricated sensor possesses excellent selectivity for detection of H_2O_2 and DA. In addition, stability was also investigated by comparisons of CVs after 100 successive assays. In this text, the oxidation current response to H_2O_2 and DA still keep up to 94.03% and 92.98% compared to that of the initial stages, implying good stability of the constructed electrode (Fig. 5b and Fig. S9b, Supplementary material). The storage stability test of constructed electrode was conducted for each 5 days at 25 °C. Compared to the initial response, no obvious current change of the electrode can be found when the experiments last 40 days, meaning ideal storage stability of this work (Fig. 5c and Fig. S9c, Supplementary material).

The reproducibility of this α-MnO_2 sensor was tested by constructing five independent electrodes in parallel, and RSD of current responses for H_2O_2 and DA are 3.42% and 3.46%, respectively. (Fig. 5d and Fig. S9d, Supplementary material). Similarly, a series of current measurements ($n = 5$) for and DA were operated on the constructed sensor, RSD is 1.9% and 1.87% (Fig. 5e and Fig. S9e, Supplementary material). Overall, the above experimental result indicated both the reproducibility and stability of the electrode constructed in this work are satisfactory.

Determination of the H_2O_2 and DA in biological samples

Finally, the sensor was employed to detect H_2O_2 and DA in biological samples including human urine and serum under optimized conditions. The samples including serum collected by centrifuged and urine were diluted 40 times with 0.05 mol·L^{-1} phosphate buffer (pH 7.4). The analyte was brought into real samples with the using of standard addition method at three different levels, in which all the experiments were conducted in triplicate. The results are depicted in Table 2, from which we can know both the recoveries of H_2O_2 and DA are all above 90%, indicating that the sensor can be successfully applied to the detection of H_2O_2 and DA in biological samples.

Conclusions

Unique hollow urchin-like structure of α-MnO_2 has been successfully synthesized by one-step hydrothermal method for 6 h when the temperature is maintained at 120 °C. Both the reaction temperature and reaction time affect the microstructure of α-MnO_2. The catalytic currents of the uniform hollow urchin-like α-MnO_2 to equal amount of H_2O_2 and DA are larger compared with other samples obtained at other reaction conditions. It may result from the uniform hollow urchin-like structure which provides a large specific surface area and more active sites. Catalytic mechanism study for H_2O_2 and DA on the sensor shows that the electrocatalysis of H_2O_2 and DA is realized in the process of different valence states transformation of Mn species. The sensor exhibits satisfactory performance, including ideal sensitivity, excellent stability and reproducibility, low detection limit, wide linear response range, short response time and high analyte specificity. It offers a potential and alternative approach for effective detection of H_2O_2 and DA.

Acknowledgments This work was supported by the National Natural Science Foundation of China (21771060, 61271126, and 21305033), International Science & Technology Cooperation Program of China (2016YFE0115100), Program for Science and Technology Project of Heilongjiang province (B2015008).

Compliance with ethical standards The author(s) declare that they have no competing interests.

References

1. Song HY, Ni YN, Kokot S (2014) Investigations of an electrochemical platform based on the layered MoS_2-graphene and horseradish peroxidase nanocomposite for direct electrochemistry and electrocatalysis. Biosens Bioelectron 56:137–143. https://doi.org/10.1016/j.bios.2014.01.014
2. Zhang C, Ren JJ, Zhou JX, Cui M, Li N, Han BK, Chen Q (2018) Facile fabrication of a 3,4,9,10-perylene tetracarboxylic acid functionalized grapheme-multiwalled carbon nanotube-gold nanoparticle nanocomposite for highly sensitive and selective electrochemical detection of dopamine. Analyst 143:3075–3084. https://doi.org/10.1039/C8AN00559A
3. He YS, Pan CG, Cao HX, Yue MZ, Wang L, Liang GX (2018) Highly sensitive and selective dual-emission ratiometric fluorescence detection of dopamine based on carbon dots-gold nanoclusters hybrid. Sensors Actuators B Chem 265:371–377. https://doi.org/10.1016/j.snb.2018.03.080
4. Begum H, Ahmed MS, Jeon S (2016) A novel δ-MnO2 with carbon nanotubes nanocomposite as an enzyme-free sensor for hydrogen peroxide electrosensing. RSC Adv 6:50572–55058. https://doi.org/10.1039/c6ra08738h
5. Mei XR, Wei QP, Long HY, Yu ZM, Deng ZJ, Meng LC, Wang J, Luo JT, Lin CT, Ma L, Zheng KZ, Hu NX (2018) Long-term stability of au nanoparticle-anchored porous boron-doped diamond hybrid electrode for enhanced dopamine detection. Electrochim Acta 271:84–91. https://doi.org/10.1016/j.electacta.2018.03.133
6. Zhuang XM, Chen DD, Zhang S, Luan F, Chen LX (2018) Reduced graphene oxide functionalized with a CoS2/ionic liquid composite and decorated with gold nanoparticles for voltammetric sensing of dopamine. Microchim Acta 185:166–173. https://doi.org/10.1007/s00604-018-2712-y

7. Chen DD, Tian CH, Li XY, Li ZH, Han ZD, Zhai C, Quan Y, Cui RJ, Zhang GH (2018) Electrochemical determination of dopamine using a glassy carbon electrode modified with a nanocomposite consisting of nanoporous platinum-yttrium and graphene. Microchim Acta 185:98–104. https://doi.org/10.1007/s00604-017-2624-2
8. Chen XY, Liu QQ, Liu MH, Zhang XY, Lin SY, Chen YS, Zhuang JY, Yang DP (2018) Protein-templated Fe2O3 microspheres for highly sensitive amperometric detection of dopamine. Microchim Acta 185:340–348. https://doi.org/10.1007/s00604-018-2876-5
9. Feng XM, Zhang Y, Song J, Chen NN, Zhou JH, Huang ZD, Ma YW, Zhang L, Wang LH (2015) MnO2/graphene nanocomposites for nonenzymatic electrochemical detection of hydrogen peroxide. Electroanalysis 27:353–359. https://doi.org/10.1002/elan.201400481
10. Zheng XY, Yu L, Lan B, Cheng G, Lin T, He BB, Ye WJ, Sun M, Ye F (2017) Three-dimensional radial a-MnO2 synthesized from different redox potential for bifunctional oxygen electrocatalytic activities. J Power Sources 362:332–341. https://doi.org/10.1016/j.jpowsour.2017.07.027
11. Park JH, Kang DC, Park SJ, Shin CH (2015) CO oxidation over MnO_2 catalysts prepared by a simple redox method: influence of the Mn (II) precursors. J Ind Eng Chem 25:250–257. https://doi.org/10.1016/j.jiec.2014.11.001
12. Jaiswal N, Tiwari I, Foster CW, Banks CE (2017) Highly sensitive amperometric sensing of nitrite utilizing bulk-modified MnO_2 decorated graphene oxide nanocomposite screen-printed electrodes. Electrochim Acta 227:255–266. https://doi.org/10.1016/j.electacta.2017.01.007
13. Mahmoudian MR, Alias Y, Basirun WJ, Woi PM, Sookhakian M (2014) Facile preparation of MnO_2 nanotubes/reduced graphene oxide nanocomposite for electrochemical sensing of hydrogen peroxide. Sensors Actuators B Chem 201:526–534. https://doi.org/10.1016/j.snb.2014.05.030
14. Ramachandran K, Zahoor A, Kumar TR, Nahm KS, Balasubramani A, Kumar GG (2017) MnO2 nanorods grown NGNF nanocomposites for the application of highly sensitive and selective electrochemical detection of hydrogen peroxide. J Ind Eng Chem 46:19–27. https://doi.org/10.1016/j.jiec.2016.09.012
15. Dong S, Xi JB, Wu YN, Liu HW, Fu CY, Liu HF, Xiao F (2015) High loading MnO_2 nanowires on graphene paper: facile electrochemical synthesis and use as flexible electrode for tracking hydrogen peroxide secretion in live cells. Anal Chim Acta 853:200–206. https://doi.org/10.1016/j.aca.2014.08.004
16. Zhuang XM, Chen DD, Wang SN, Liu HT, Chen LX (2017) Manganese dioxide nanosheet-decorated ionic liquid-functionalized graphene for electrochemical theophylline biosensing. Sensors Actuators B Chem 251:185–191. https://doi.org/10.1016/j.snb.2017.05.049
17. Li JH, Jiang JB, Liu MQ, Xu ZF, Deng PH, Qian D, Tong CY, Xie HB, Yang CM (2017) Facile synthesis of MnO2-embedded flower-like hierarchical porous carbon microspheres as an enhanced electrocatalyst for sensitive detection of caffeic acid. Anal Chim Acta 985:155–165. https://doi.org/10.1016/j.aca.2017.07.002
18. Li ZQ, Ding Y, Xiong YJ, Yang Q, Xie Y (2005) One-step solution-based catalytic route to fabricate novel a-MnO_2 hierarchical structures on a large scale. Chem Commun 7:918–920. https://doi.org/10.1039/B414204G
19. He SJ, Zhang BY, Liu MM, Chen W (2014) Non-enzymatic hydrogen peroxide electrochemical sensor based on a three dimensional MnO_2 nanosheets/carbon foam composite. RSC Adv 4:49315–49323. https://doi.org/10.1039/c4ra09007a
20. He QG, Liang J, Li GL, Deng PH, Liu J, Liu XP (2018) Electrochemical detection of dopamine based on MnO2 nanowires/reduced graphene oxide composites modified glassy carbon electrode. Chinese. J Anal Chem 46:438–445. https://doi.org/10.11895/j.issn.0253.3820.171183
21. Wu NT, Du WZ, Gao X, Zhao L, Liu GL, Liu XM, Wu H, He YB (2018) Hollow SnO2 nanospheres with oxygen vacancies entrapped by a N-doped graphene network as robust anode materials for lithium-ion batteries. Nanoscal 10(24):11460–11466. https://doi.org/10.1039/c8nr02290a
22. Ensafi AA, Moosavifard SE, Rezaei B, Kaverlavani SK (2018) Engineering onion-like nanoporous CuCo2O4 hollow spheres derived from bimetal-organic frameworks for high-performance asymmetric supercapacitors. J Mater Chem A 6(22):10497–10506. https://doi.org/10.1039/C8TA02819B
23. Zhang WX, Zeng CY, Kong M, Pan YM, Yang ZH (2012) Water-evaporation-induced self-assembly of -MnO_2 hierarchical hollow nanospheres and their applications in ammonia gas sensing. Sensors Actuators B Chem 162:292–299. https://doi.org/10.1016/j.snb.2011.12.080
24. Zakaria ABM, Leszczynska D (2016) Novel design of non-enzymatic sensor for rapid monitoring of hydrogen peroxide in water matrix. J Electroanal Chem 766:30–36. https://doi.org/10.1016/j.jelechem.2016.01.027
25. Yang BB, Wang J, Bin D, Zhu MS, Yang P, Du YK (2015) A three dimensional Pt nanodendrite/graphene/MnO2 nanoflower modified electrode for the sensitive and selective detection of dopamine. J Mater Chem 3:7440–7448. https://doi.org/10.1039/c5tb01031d
26. Gao L, Zhu MZ, Xia T, Li Q, Li TS, Zhao H (2018) Ni-doped BaFeO3-δ perovskite oxide as highly active cathode electrocatalyst for intermediate-temperature solid oxide fuel cells. Electrochim Acta 289:428–436. https://doi.org/10.1016/j.electacta.2018.09.096
27. Liu LH, You W, Zhan XM, Gao ZN (2014) Electrochemical behavior of lansoprazole at a multiwalled carbon nanotubes-ionic liquid modified glassy carbon electrode and its electrochemical determination. J Serb Chem Soc 79:39–52. https://doi.org/10.2298/JSC121216059L
28. Wu ZL, Li CK, Yu JG, Chen XQ (2017) MnO2/reduced graphene oxide nanoribbons: facile hydrothermalpreparation and their application in amperometric detection ofhydrogen peroxide. Sensors Actuators B Chem 239:544–552. https://doi.org/10.1016/j.snb.2016.08.062
29. Zhang J, Rao DJ, Zheng JB (2016) Synthesis of ag nanoparticle doped MnO2/GO nanocomposites at a gas/liquid Interface and its application in H2O2 detection. Electroanalysis 28:588–595. https://doi.org/10.1002/elan.201500398
30. Cui SF, Li Y, Deng DM, Zeng LL, Yan XX, Qian J, Luo LQ (2016) Photo-reduction assisted synthesis of MnO2/reduced graphene oxide/P25 for electrochemical detection of hydrogen peroxide. RSC Adv 6:2632–2640. https://doi.org/10.1039/c5ra13275d
31. Xu B, Ye ML, Yu YX, Zhang WD (2010) A highly sensitive hydrogen peroxideamperometric sensor based on MnO_2-modified vertically aligned multiwalledcarbon nanotubes. Anal Chim Acta 674:20–26. https://doi.org/10.1016/j.aca.2010.06.004
32. Divagar M, Sriramprabha R, Ponpandian N, Viswanathan C (2018) Highly selective and sensitive electrochemical detection of dopamine with hydrothermally prepared beta-MnO_2 nanostructures. Mater Sci Semicond Process 83:216–223. https://doi.org/10.1016/j.mssp.2018.04.034
33. Shoja Y, Rafati AA, Ghodsi J (2017) Polythiophene supported MnO2 nanoparticles as nano-stabilizer for simultaneously electrostatically immobilization of D-amino acid oxidase and hemoglobin as efficient bio-nanocomposite in fabrication of dopamine bi-enzyme biosensor. Mat Sci Eng C - Mater 76:637–645. https://doi.org/10.1016/j.msec.2017.03.155
34. Yang BB, Wang J, Bin D, Zhu MS, Yang P, Du YK (2015) A three dimensional Pt nanodendrite/graphene/MnO2 nanoflower modified

electrode for the sensitive and selective detection of dopamine. J Mater Chem B 3:7440–7448. https://doi.org/10.1039/C5TB01031D

35. Sáenz HSC, Hernández-Saravia LP, Selva JS, Sukeri A, Espinoza-Montero PJ, Bertotti M (2018) Electrochemical dopamine sensor using a nanoporous gold microelectrode: a proof-of-concept study for the detection of dopamine release by scanning electrochemical microscopy. Microchim Acta 185:367–375. https://doi.org/10.1007/s00604-018-2898-z
36. Khan MZH, Liu XQ, Tang YF, Zhu JH, Hu WP, Liu XH (2018) A glassy carbon electrode modified with a composite consisting of gold nanoparticle, reduced graphene oxide and poly(L-arginine) for simultaneous voltammetric determination of dopamine, serotonin and L-tryptophan. Microchim Acta 185:439–448. https://doi.org/10.1007/s00604-018-2979-z
37. Song XJ, Fu J, Wang J, Li CY, Liu ZH (2018) Simultaneous voltammetric determination of acetaminophen and dopamine using a glassy carbon electrode modified with copper porphyrin-exfoliated graphene. Microchim Acta 185:369–376. https://doi.org/10.1007/s00604-018-2891-6